Supplement of Atmos. Chem. Phys., 24, 7731–7754, 2024
https://doi.org/10.5194/acp-24-7731-2024-supplement

Atmospheric Chemistry and Physics
Open Access
EGU

Supplement of

Diverse sources and aging change the mixing state and ice nucleation properties of aerosol particles over the western Pacific and Southern Ocean

Jiao Xue et al.

Correspondence to: Jiyeon Park (jypark@kopri.re.kr) and Bingbing Wang (bingbing.wang@xmu.edu.cn)

Section S1.

During the sample collection, we need a suitable particle loading on the substrates for the single particle analysis and ice nucleation experiments. A good particle loading with sufficient particles should be achieved for single particle analysis to obtain statistically significant information. Over-loaded sampling and particle aggregation should be avoided. Thus, we adjusted the sampling time according to the particle concentrations in different regions during the field campaign. As shown in Table S1, close to the continent of East Asia, the sampling time was 10 min for S1 to S4. From S5 to S20, the sampling time was about 240 min. Over the SO region, the sampling time was about 360 min for S21 to S29.

Section S2

Ice nucleation activated fraction

We report the ice nucleation activated fraction as the ratio between the number of particles that nucleated ice to the total particle number available for each ice nucleation experiment (i.e., the number of particles deposited). The number of ice crystals determined by OM images is typically one to three ice crystals at the onsets. IN-activated fractions of each sample were summarized in Table 1. It ranges from 0.01‰ to 0.24‰ with the maximum value appearing in S1. It should be noted that the IN-activated fraction determined here should be interpreted as a higher limit at the ice nucleation onset conditions since the number of small particles deposited on the substrate can be underestimated by optical microscopy (OM).

Ice nucleation active site density (n_s)

The singular hypothesis (SH) assumes that heterogeneous ice nucleation occurs on active sites located on the particle surface where one active site can form one single ice crystal (Vali, 1971; Connolly et al., 2009). n_s is temperature dependent and time independent. Having units of cm^{-2}, n_s is defined as $n_s = N_{ice}/A_{tot}$, where N_{ice} is the number of the observed ice nucleation events that occurred in a temperature interval and A_{tot} is the total particle surface area available for ice nucleation experiment. In this study, the interval of 0.02 K was applied corresponding to the temperature difference between the recorded subsequent OM images. The ensemble of experiments at similar T_d were combined for analysis. Experimentally derived for n_s DIN and IMF as a function of temperature for different types of samples are presented in Fig. S17. n_s

demonstrates a strong temperature dependence increasing by about 1 – 2 orders of magnitude as temperature decreases within a few degrees. The parameterizations for n_s as a function of temperature are provided in Table S2. For DIN, the Dust dominated sample demonstrated the highest median n_s of about 2×10^3 cm^{-2} whereas the BBA influenced sample had the lowest median n_s of about 5×10^2 cm^{-2}. This suggests that particles of the Dust dominated sample are more efficient INPs than the particles of the BBA influenced sample. We provide the exponential fits (solid lines) for n_s as a function of temperature (T), $n_s = 10^{(a\times T+b)}$, at different temperature ranges (Fig. S17). Values of a and b are listed in Table S3. Compared with the other samples, the a (negative value) is larger for the FreshSS and AgedSS dominated samples indicating a weaker dependence of n_s on temperature. Fig. S18 shows the median n_s with 25th and 75th percentiles for all types of samples.

Heterogeneous ice nucleation rate coefficient (J_{het})

The uncertainty of J_{het} has contributions from stochastic freezing (statistical uncertainty) or the number of ice nucleation events, and the uncertainty in temperature, RH_{ice}, and surface area. We followed the method by Alpert and Knopf and quantified the total uncertainty of J_{het} in the form of $\Delta J_{het} = J_{het}\,^{\times k}_{\div j}$, indicating the upper and lower limits of a factor k times higher or j times lower (Alpert and Knopf, 2016; China et al., 2017). Statistical uncertainty for the Dust, BBA, CNOS and SS/Sulf, and the FreshSS and AgedSS dominated samples were $J_{het}\,^{\times 39}_{\div 6}$, $J_{het}\,^{\times 48}_{\div 6}$, $J_{het}\,^{\times 22}_{\div 5}$, and $J_{het}\,^{\times 7}_{\div 3}$, respectively. ΔJ_{het} for IMF of FreshSS and AgedSS dominated samples were $J_{het}\,^{\times 61}_{\div 6}$. ΔJ_{het} from a temperature uncertainty of ± 0.3 K were $J_{het}\,^{\times 2}_{\div 2}$. ΔJ_{het} from the maximum RH_{ice} uncertainty of ± 11% were $J_{het}\,^{\times 10^{0.11c}}_{\div 10^{0.11c}}$, where c is one of the parameters for J_{het} parameterizations in Table 2. If considering the uncertainty of about a factor of 2 in surface area, ΔJ_{het} was $J_{het}\,^{\times 2}_{\div 2}$. Combining all the uncertainties, the DIN ΔJ_{het} of the Dust, BBA, CNOS and SS/Sulf, and the FreshSS and AgedSS dominated samples were $J_{het}\,^{\times 45}_{\div 12}$, $J_{het}\,^{\times 55}_{\div 13}$, $J_{het}\,^{\times 28}_{\div 11}$, and $J_{het}\,^{\times 13}_{\div 9}$, respectively. The IMF J_{het} of the FreshSS and AgedSS dominated samples was $J_{het}\,^{\times 297}_{\div 17}$.

In our previous study, θ was parameterized as a function of RH_{ice} including a set of various particle types (Wang and Knopf, 2011). θ for various particle types fall tightly into the parameterization. Here, we propose new parameterizations of θ as a function of $T^3\ln[RH_{ice}]^2$ to include the ice

nucleation onset temperature and RH_{ice}, represented by $\theta = a + b \times \ln(T^3 \ln[RH_{\mathrm{ice}}]^2 + c)$. As shown in Fig. S17, θ for the same particle types shows very similar trends. All fitting correlation coefficients, R^2, were larger than 0.99. The values of a, b, and c for each parameterization are listed in Fig. S17. It is worth noting that the parameterization only applies to the DIN.

Section S3

NaCl particles were generated by nebulizing NaCl solution and passing through a silicone dryer to form particles. NaCl particles were collected on silicon wafers for ice nucleation experiments. The surface area range of NaCl samples was 1.0×10^4 to 13.2×10^4 μm^2 with the particle size range of 1 – 4.5 μm, which was comparable to the investigated field samples.

Table S1. Information for the particle samples collected aboard the R/V *Araon* including the collecting date, time, and location; collection time (sampling duration); the mean values (average) of air temperature, relative humidity (RH), air pressure, black carbon (BC) concentration and relative wind speed; and the range of relative wind direction. The number of particles examined by CCSEM/EDX was listed and the samples used for ice nucleation experiments were marked.

Region	Samples ID	Collecting start time (UTC)	Collecting end time (UTC)	Collection Time (mins)	Collecting start location (latitude, longitude)	Collecting end location (latitude, longitude)	Average air temperature (℃)	Average RH (%)	Average Pressure (hPa)	Average relative wind speed (m/s)	Relative wind direction range (°)	Average BC concentration (ng/m3)	Number of particles examined by CCSEM	Ice nucleation experiment
WP-I	S1	10/31 19:19	10/31 19:29	10	34.96° N, 125.61° E	34.93° N, 125.61° E	18.6±0.0	85.5±0.2	1017.6±0.0	07.1±0.3	68 - 75	1963.3±42.0	1270	√
	S2	11/01 20:57	11/01 21:07	10	30.29° N, 128.67° E	30.26° N, 128.69° E	22.4±0.1	56.4±1.6	1014.1±0.0	09.8±0.3	357 - 9	217.0±127.5	910	
	S3	11/02 21:52	11/02 22:02	10	25.59° N, 131.56° E	25.57° N, 131.57° E	26.5±0.0	80.3±0.5	1009.8±0.1	14.1±0.1	337 - 342	189.8±174.2	1002	
	S4	11/03 21:06	11/03 21:16	10	21.90° N, 134.75° E	21.87° N, 134.77° E	27.7±0.0	80.2±0.2	1007.9±0.0	12.4±0.2	355 - 358	9.2±9.8	914	√
	S5	11/03 21:33	11/04 01:33	240	21.83° N, 134.81° E	21.12° N, 135.28° E	28.0±0.2	77.0±2.6	1007.1±0.2	10.0±0.4	337 - 4	25.9±15.4	1191	
	S6	11/04 23:14	11/05 03:14	240	17.23° N, 137.58° E	16.40° N, 138.29° E	28.6±0.4	80.2±2.2	1001.3±0.8	11.2±1.6	305 - 325	35.9±46.4	928	
	S7	11/05 23:48	11/06 03:48	240	13.03° N, 141.09° E	12.36° N, 141.56° E	28.8±0.2	77.9±1.5	1000.4±0.8	05.9±0.5	346 - 22	22.2±30.3	908	
WP-II	S8	11/08 02:01	11/08 06:07	246	04.26° N, 147.22° E	03.45° N, 147.54° E	29.3±0.1	76.5±2.0	1003.4±0.5	13.4±1.5	67 - 80	107.4±70.6	1247	
	S9	11/08 08:00	11/08 12:00	240	03.25° N, 148.09° E	02.43° N, 148.42° E	29.2±0.1	80.4±1.9	1005.2±0.7	10.7±0.7	11 - 67	50.3±31.5	1064	
	S10	11/08 13:00	11/08 17:00	240	02.32° N, 148.50° E	01.51° N, 149.22° E	28.8±0.1	81.5±1.6	1004.9±0.6	07.2±1.7	347 - 20	17.6±13.3	986	√
	S11	11/10 05:31	11/10 10:04	273	04.45° S, 154.02° E	05.46° S, 154.12° E	28.1±0.3	79.4±2.9	1005.0±0.8	08.1±1.6	326 - 10	26.3±29.8	1075	√
	S12	11/11 05:04	11/11 09:04	240	09.12° S, 155.36° E	10.02° S, 156.02° E	28.2±0.5	72.8±5.6	1005.1±0.8	16.9±0.7	359 - 15	60.9±47.1	1409	√
	S13	11/12 05:01	11/12 09:01	240	13.30° S, 157.55° E	14.11° S, 158.17° E	27.3±0.1	68.1±1.5	1007.1±0.9	16.4±0.4	353 - 5	161.5±50.1	979	
	S14	11/13 03:47	11/13 07:49	242	17.19° S, 160.01° E	18.02° S, 160.25° E	25.7±0.1	64.3±1.4	1007.8±0.4	13.6±0.3	352 - 3	674.7±59.3	966	√
	S15	11/14 03:38	11/14 07:38	240	20.59° S, 162.04° E	21.47° S, 162.21° E	23.5±0.1	62.6±1.2	1009.5±0.4	12.2±0.4	1 - 22	356.8±122.9	1483	
	S16	11/14 20:39	11/15 00:39	240	24.29° S, 163.03° E	25.20° S, 163.12° E	22.1±0.1	74.1±0.8	1013.0±0.2	07.7±1.2	331 - 353	31.1±20.0	1027	
	S17	11/17 19:31	11/17 23:31	240	37.13° S, 169.01° E	37.52° S, 169.39° E	14.7±0.7	78.7±4.7	1008.2±0.2	09.9±2.9	69 - 112	30.4±31.5	730	
SO	S18	11/28 19:15	11/28 23:15	240	61.33° S, 174.10° W	62.17° S, 173.58° W	1.7±0.5	97.9±0.3	982.9±0.2	11.8±2.5	26 - 344	52.1±81.2	666	
	S19	11/29 07:28	11/29 11:28	240	63.52° S, 173.16° W	64.38° S, 172.58° W	-0.9±0.2	93.8±0.7	966.8±7.3	17.9±1.4	325 - 341	65.6±106.6	794	
	S20	11/29 19:43	11/29 23:43	240	66.14° S, 172.17° W	66.55° S, 171.59° W	-3.5±0.1	88.1±1.6	973.5±5.7	13.3±1.4	323 - 11	4.4±5.6	1011	√
	S21	12/01 04:26	12/01 10:30	364	71.18° S, 171.49° W	72.04° S, 172.07° W	-4.6±0.4	80.9±6.9	992.0±1.3	07.8±0.7	3 - 356	36.3±6.0	992	
	S22	12/02 05:46	12/02 11:47	361	73.26° S, 176.20° W	74.21° S, 178.58° E	-4.2±1.1	81.9±14.4	990.7±14.0	09.3±5.2	19 - 61	17.0±88.4	924	
	S23	12/02 16:00	12/02 22:02	362	74.07° S, 177.09° W	75.12° S, 173.34° E	-2.2±0.3	75.8±2.8	984.1±1.0	13.2±2.4	349 - 49	3.5±20.2	978	
	S24	12/03 01:55	12/03 07:53	358	75.08° S, 171.07° E	74.55° S, 166.26° E	-2.3±0.2	69.1±0.2	963.9±0.7	15.6±1.7	8 - 67	59.2±28.3	638	
	S25	12/08 21:18	12/09 03:21	363	74.43° S, 164.49° E	74.59° S, 169.33° E	-2.7±0.2	79.2±2.1	993.4±0.3	07.5±1.1	7 - 359	14.9±20.4	861	
	S26	12/09 08:26	12/09 14:26	360	74.57° S, 173.14° E	74.18° S, 177.20° E	-3.2±0.7	79.6±3.4	990.4±0.7	11.0±2.6	305 - 331	14.3±36.9	944	
	S27	12/09 19:48	12/10 01:49	361	73.42° S, 179.06° W	73.07° S, 175.26° W	-4.3±0.4	85.7±3.9	992.7±0.5	09.0±2.4	344 - 36	25.4±54.5	928	√
	S28	12/10 19:56	12/11 01:58	362	70.39° S, 171.00° W	69.34° S, 171.11° W	-4.1±0.1	68.6±2.9	993.9±1.0	12.3±1.8	19 - 108	38.7±21.5	922	
	S29	12/11 20:03	12/12 02:03	360	66.59° S, 178.24° W	66.24° S, 179.52° E	-0.3±0.4	98.6±6.0	980.2±9.4	11.8±1.9	0 - 359	36.3±62.4	814	

Table S2. Enrichment factors for different types of INPs. The lower and upper limits of *EF*s were calculated by Poisson distribution at 95% confidence level.

EF	FrehsSS	AgedSS	SS/Sulf	CNOS	CNO	Dust	Mixture	Aging process
WP-I-S1	\	$0.89^{2.29}_{0.24}$	$2.53^{6.53}_{0.69}$	$1.09^{2.83}_{0.30}$	$0.00^{1.64}_{0.00}$	$1.48^{2.68}_{0.74}$	$0.45^{1.41}_{0.08}$	$1.31^{2.59}_{0.57}$
WP-II-S14	\	$0.00^{1.03}_{0.00}$	$2.75^{13.05}_{0.14}$	$1.57^{4.95}_{0.28}$	$1.34^{2.23}_{0.75}$	$0.00^{16.48}_{0.00}$	$0.48^{2.27}_{0.02}$	$0.31^{1.45}_{0.02}$
WP-II-S10	\	$0.00^{1.59}_{0.00}$	$1.52^{2.21}_{1.01}$	$1.03^{2.17}_{0.41}$	\	$0.00^{8.35}_{0.00}$	$0.17^{0.83}_{0.01}$	$1.33^{1.93}_{0.88}$
WP-I-S4	$0.95^{1.66}_{0.50}$	$0.91^{1.60}_{0.48}$	$2.72^{5.72}_{1.07}$	$0.00^{8.15}_{0.00}$	$0.00^{32.58}_{0.00}$	$2.18^{10.32}_{0.11}$	$0.00^{1.55}_{0.00}$	$1.20^{1.87}_{0.72}$
WP-II-S11	$0.52^{1.63}_{0.09}$	$1.06^{1.66}_{0.64}$	$2.17^{4.57}_{0.86}$	$0.00^{8.14}_{0.00}$	$2.72^{12.88}_{0.14}$	$0.00^{32.55}_{0.00}$	$0.00^{1.63}_{0.00}$	$1.23^{1.80}_{0.80}$
WP-II-S12	$0.94^{1.65}_{0.49}$	$1.14^{1.75}_{0.70}$	$0.00^{2.75}_{0.00}$	$5.50^{26.09}_{0.28}$	$0.00^{32.96}_{0.00}$	$0.00^{16.48}_{0.00}$	$0.58^{2.75}_{0.03}$	$1.05^{1.62}_{0.65}$
All INPs	$0.88^{5.25}_{0.57}$	$0.93^{4.95}_{0.70}$	$1.86^{9.22}_{1.24}$	$0.90^{20.12}_{0.61}$	$1.09^{7.42}_{0.66}$	$1.21^{9.92}_{0.75}$	$0.28^{2.54}_{0.11}$	$1.26^{5.84}_{0.95}$

Note: '\' indicates that there was no such class in all particles.

Table S3. The a and b values in the parameterizations of n_s for the DIN and IMF, $n_s = 10^{(a \times T + b)}$.

Temperature	Type	a	b
205K-DIN	FreshSS+AgedSS	– 0.46	98.38
210K-DIN	Dust	– 1.08	229.50
	BBA	– 0.93	197.79
	CNOS+SS/Sulf	– 0.33	72.72
	FreshSS+AgedSS	– 0.45	96.37
215K-DIN	Dust	– 1.89	410.07
	BBA	– 1.05	228.38
	CNOS+SS/Sulf	– 2.35	505.43
	FreshSS+AgedSS	– 0.55	121.04
220K-DIN	Dust	– 0.73	163.69
	BBA	– 3.34	738.29
	CNOS+SS/Sulf	– 2.65	587.31
	FreshSS+AgedSS	– 0.32	72.87
225K-DIN	Dust	– 1.62	368.58
	BBA	– 1.29	293.44
	CNOS+SS/Sulf	– 1.40	317.75
225K-IMF	FreshSS+AgedSS	– 0.89	204.49
230K-DIN	Dust	– 1.42	328.27
	BBA	– 1.47	340.32
235K-DIN	Dust	– 0.54	130.47

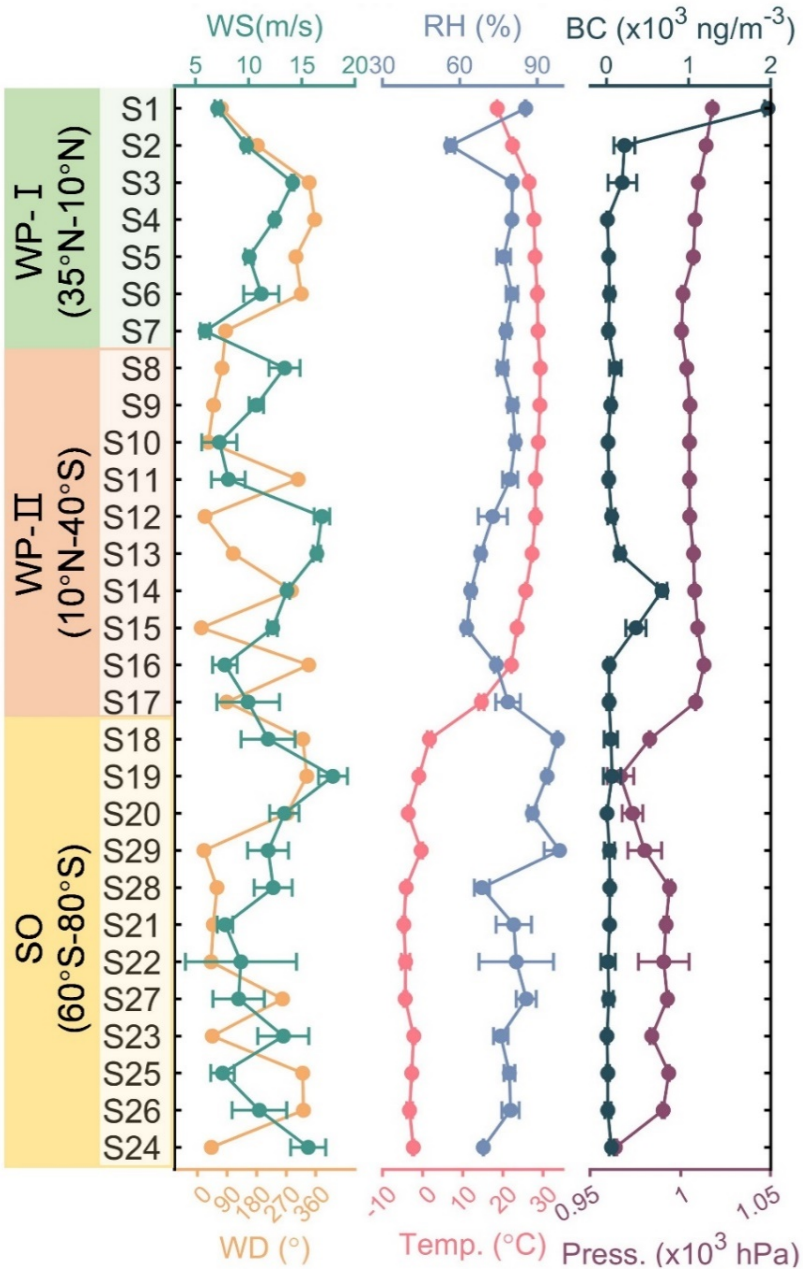

Figure S1. Meteorological data and BC concentrations for all samples. Mean values with one standard deviation for the relative wind speed (WS), relative wind direction (WD), air temperature (Temp.), RH, pressure (Press.), and BC concentration. Samples of S1 – S7, S8 – S17, and S18 – S24 were located in 35°N – 10°N, 10°N – 40°S, and 60°S – 80°S regions, respectively.

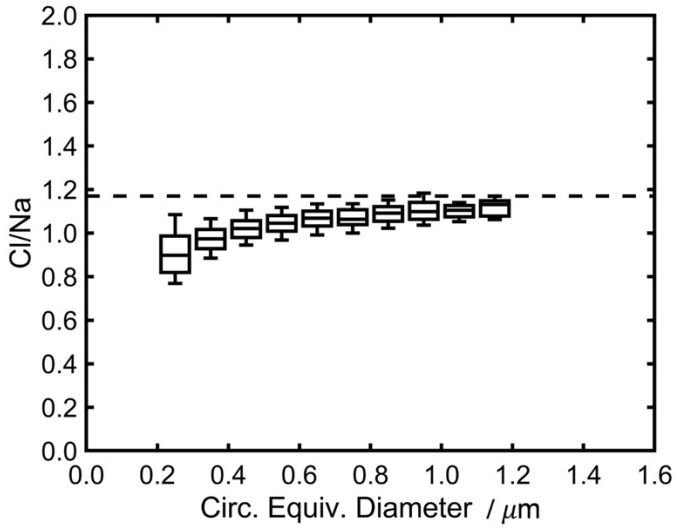

Figure S2. The Cl/Na of NaCl particles and fresh sea salt particles by nebulizing seawater based on CCSEM/EDX analysis. The Cl/Na was slightly higher than 0.8 for particles at about 0.3 μm. This is partially due to electron beam damage on small particles. The Cl/Na increases as particle size increases close to the Cl/Na of 1.17 in seawater. This is consistent with previous studies using CCSEM/EDX analysis on NaCl particles (Laskin et al., 2012; Ghorai et al., 2014).

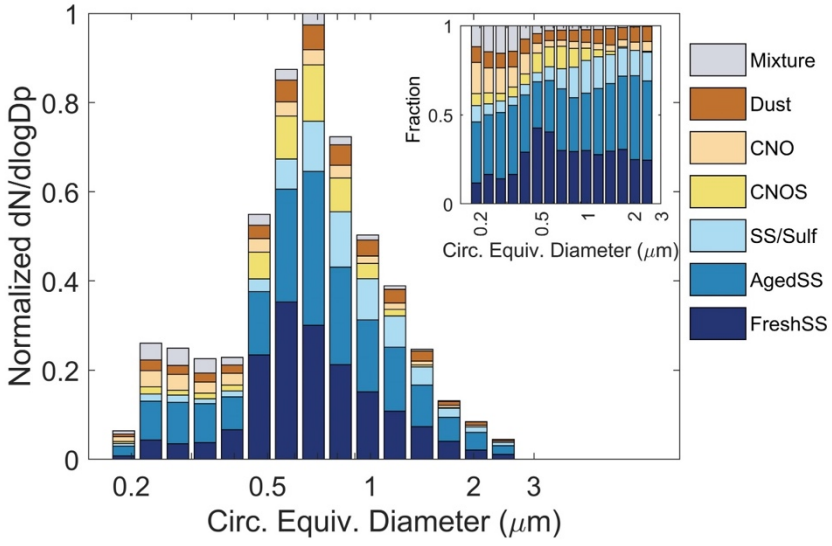

Figure S3. The size distribution of all types of particles for all samples. The inset plot shows the fractions of all types of particles.

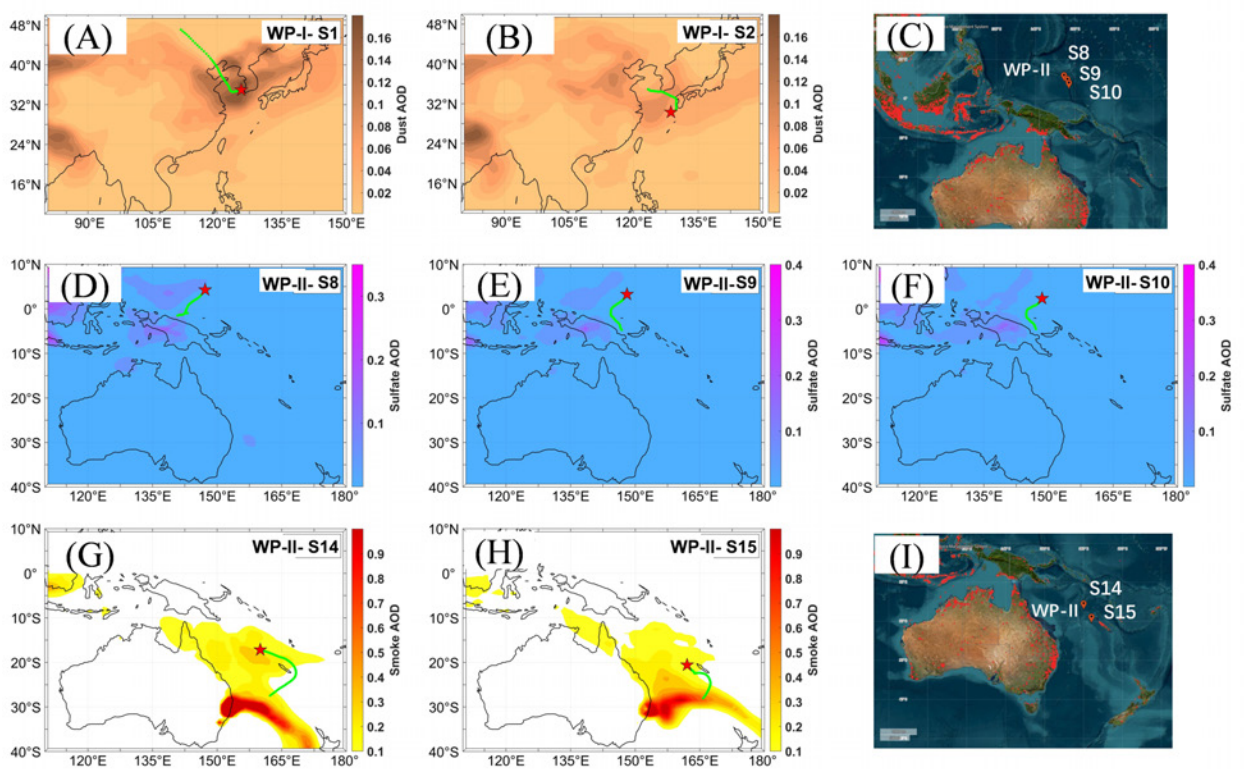

Figure S4. Aerosol optical depth (AOD) of dust (A and B), sulfates (D – F), and smoke (G and H) produced by Navy Aerosol Analysis and Prediction System reanalysis (NAAPS-RA, at 550nm) overlaid with HYSPLIT 72h backward trajectories (green line). (C) and (I) are the accumulated fire spots from Nov. 2nd to Nov. 8th, 2019 and from Nov. 8th to 14th, 2019, respectively, from Fire Information for Resource Management System (FIRMS). Sample labels are shown on the top right of each panel.

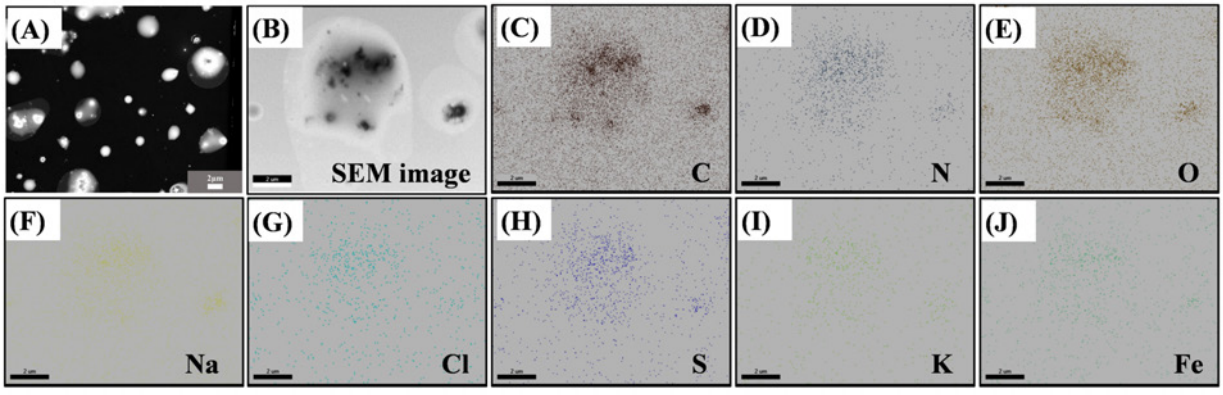

Figure S5. SEM images (A and B) and EDX elemental maps (C – J) indicate characteristics of BBA particles from S14 sample. (A) SEM image of a larger field was captured on the darkfield mode using scanning transmission electron microscopy (STEM) detector. (B) SEM image of a smaller field for chemical mapping (C – J) by collecting EDX signals. Intense carbon signals within the particle (B) indicated high density of carbon inclusions which likely are aged soot. The scale bar for all images is 2 µm.

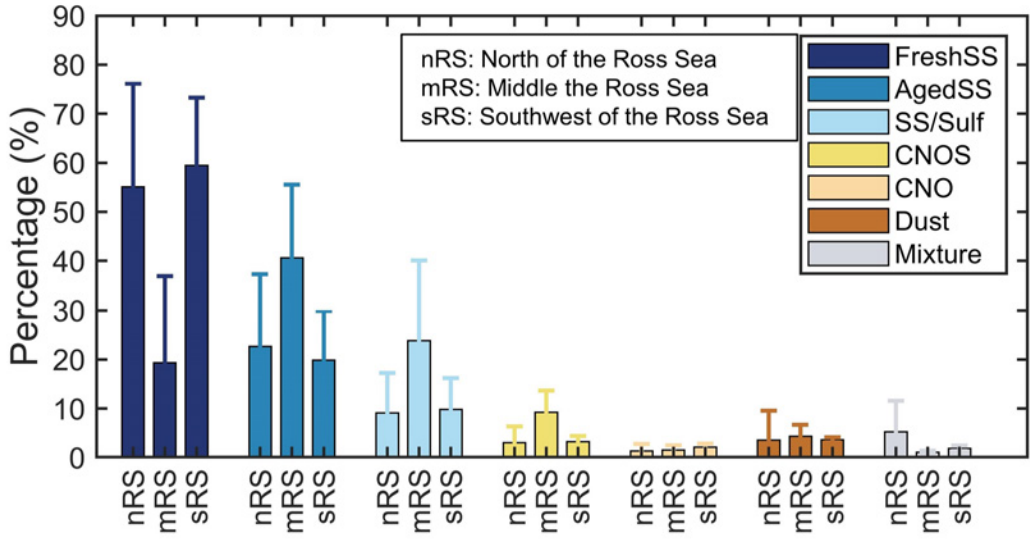

Figure S6. The average number percentages of all particle classes for samples that were collected in the middle of Ross Sea (S28, S21, S22, S27, and S23), the north part of Ross Sea (S18, S19, S20, and S29), and the southwest part of Ross Sea (S25, S26, and S24).

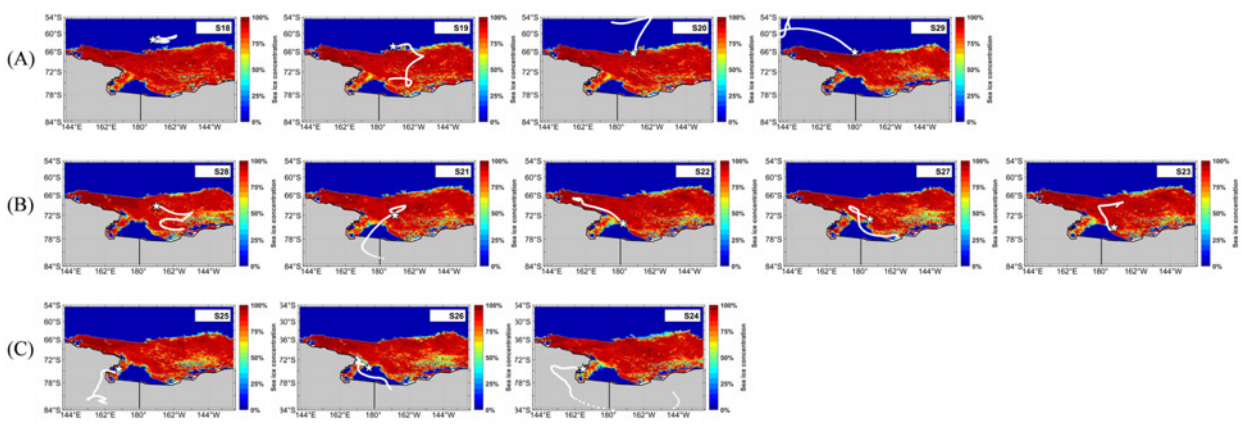

Figure S7. Sea ice concentration over the third sample region (SO) (data retrieved from https://seaice.uni-bremen.de/sea-ice-concentration/amsre-amsr2/) overlaid with HYSPLIT 120 h backward trajectories (white lines). The stars represent the sampling locations. The sample number is shown in the upper right corner of each panel. (A) north of the Ross Sea (S18, S19, S20, and S29), (B) middle of the Ross Sea (S28, S21, S22, S27, and S23), (C) southwest of the Ross Sea (S28, S21, S22, S27, and S23).

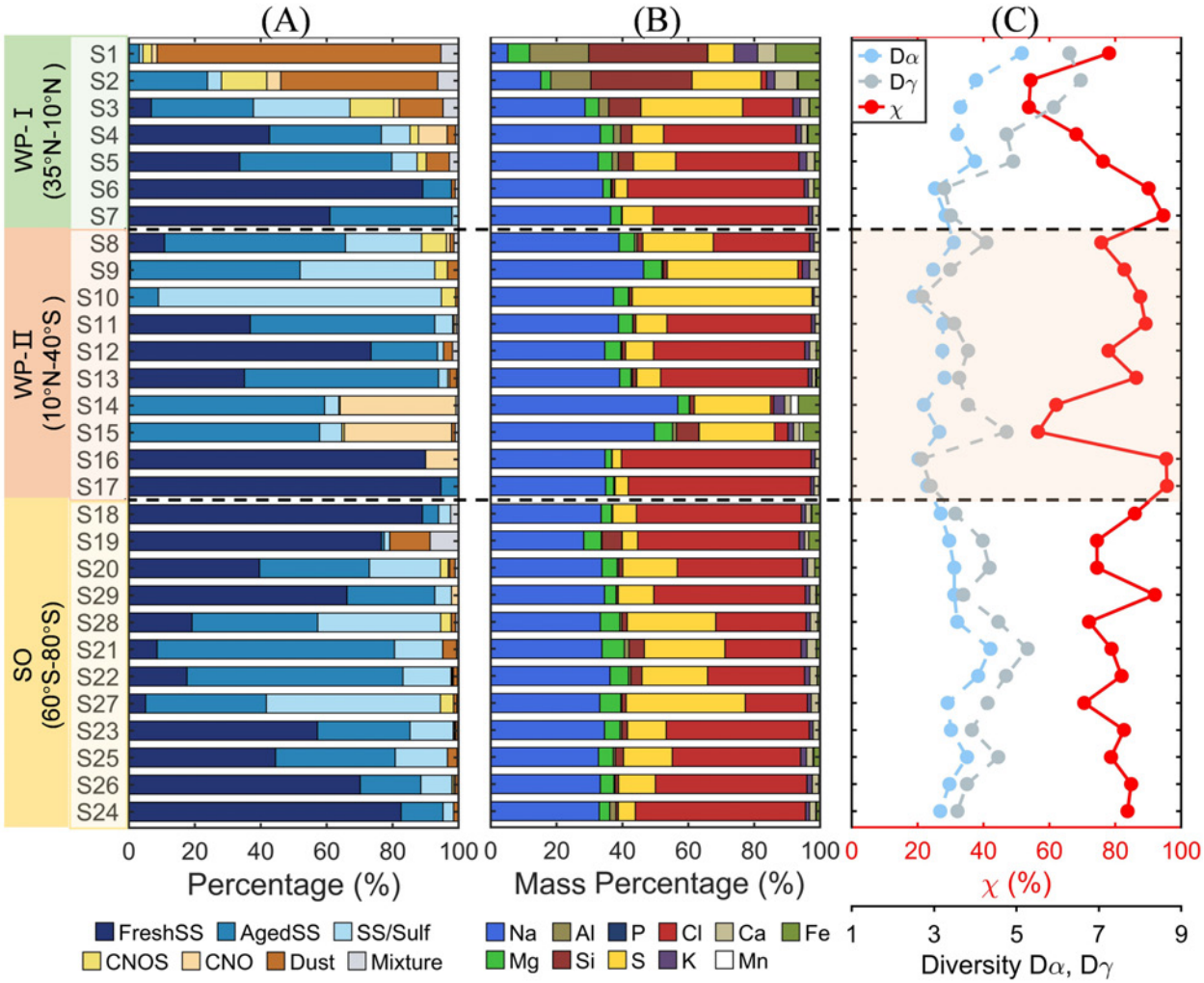

Figure S8. The number percentages of different particle classes (A), mass percentages of elements (B), and mixing state (C) of super-micron particles (diameter > 1 μm). Light blue, gray, and red points represent the average particle elemental diversity (D_α), bulk population elemental diversity (D_γ), and mixing state index (χ), respectively.

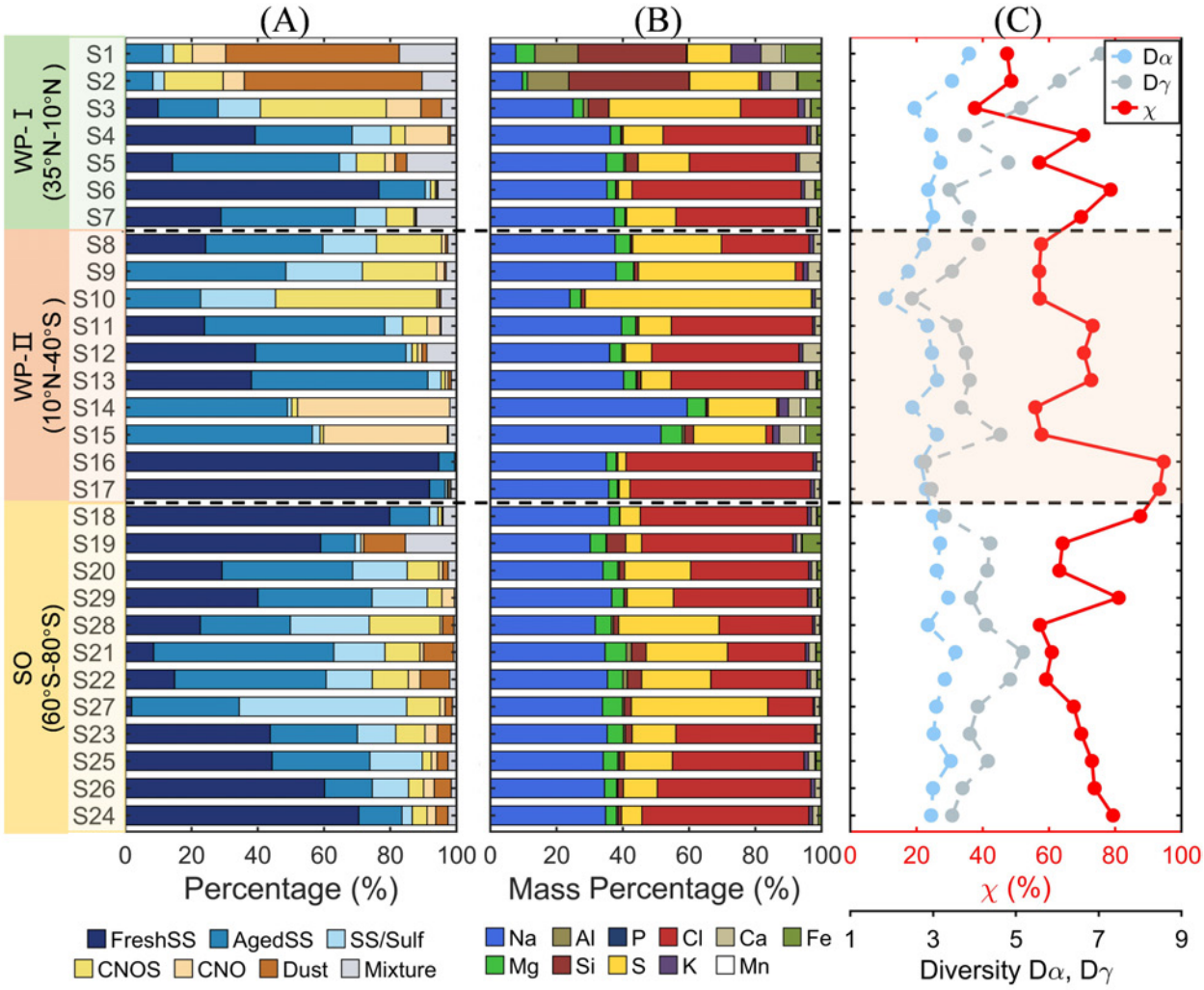

Figure S9. The number percentages of different particle classes (A), mass percentages of elements (B), and mixing state (C) of submicron particles (diameter between 0.2 and 1 μm). The light blue, gray, and red points represent D_{α}, D_{γ}, and χ, respectively.

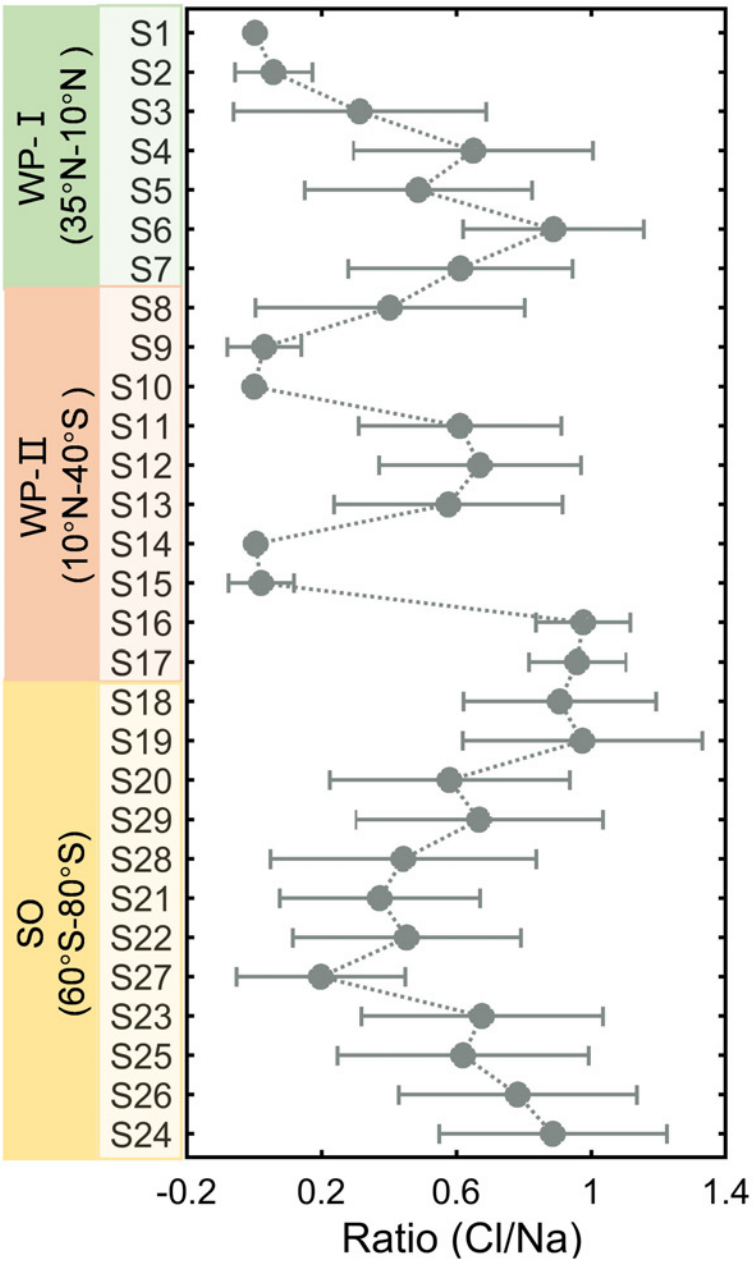

Figure S10. The ratio of chlorine to sodium in FreshSS, AgedSS, and SS/Sulf particles. The data are mean values with one standard deviation.

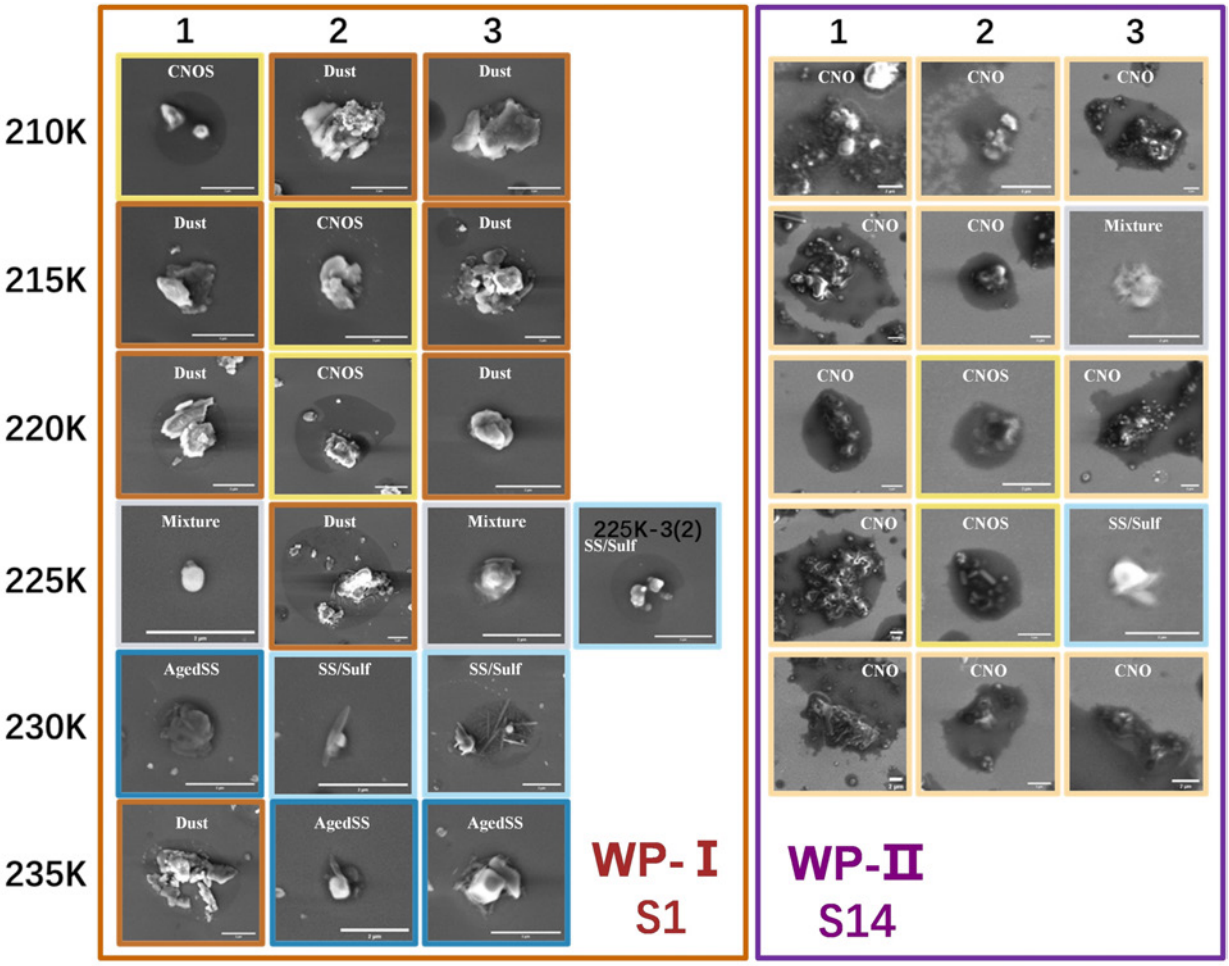

Figure S11. SEM images of INPs of the Dust dominated samples (S1) and BBA influenced samples (S14) identified at different freezing temperatures. The frame color of images represents the types of INPs and uses the same color codes in Figure 2. Blue, light blue, yellow, light orange, brown, and gray represent the FreshSS, AgedSS, SS/Sulf, CNOS, CNO, Dust, and Mixture particle classes, respectively. The number on top represents the sequence of ice nucleation experiments. The number on the SEM image indicates the temperature and number of INPs at the onset conditions. For example, the label "225K-3(2)" means this is the second INP nucleated ice at the same RH_{ice} for the 3rd ice nucleation experiment at 225 K. The scale bar for all images is 2μm.

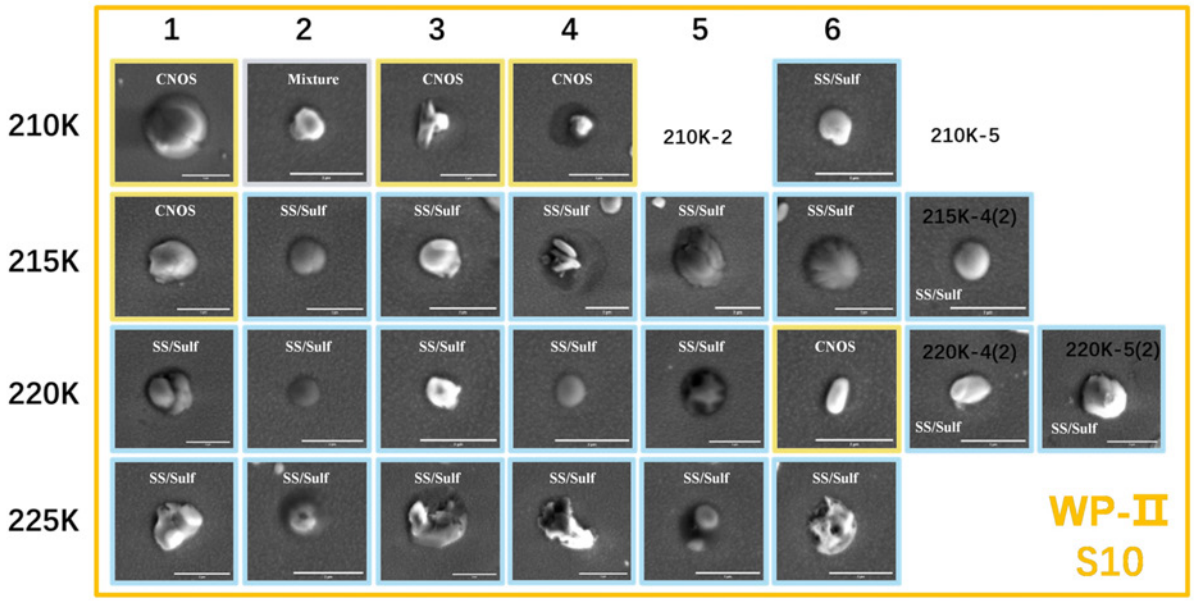

Figure S12. SEM images of INPs of the CNOS and SS/Sulf dominated sample (S10) identified at different freezing temperatures. The label without SEM image indicates the same INP nucleated ice at a different ice nucleation experiment at the same temperature. For example, the label "210K-2" means at the fifth ice nucleation experiment the INP is the same as the second run at 210 K. Other descriptions of the labels are the same as in Figure S11. The scale bar for all images is 2 μm.

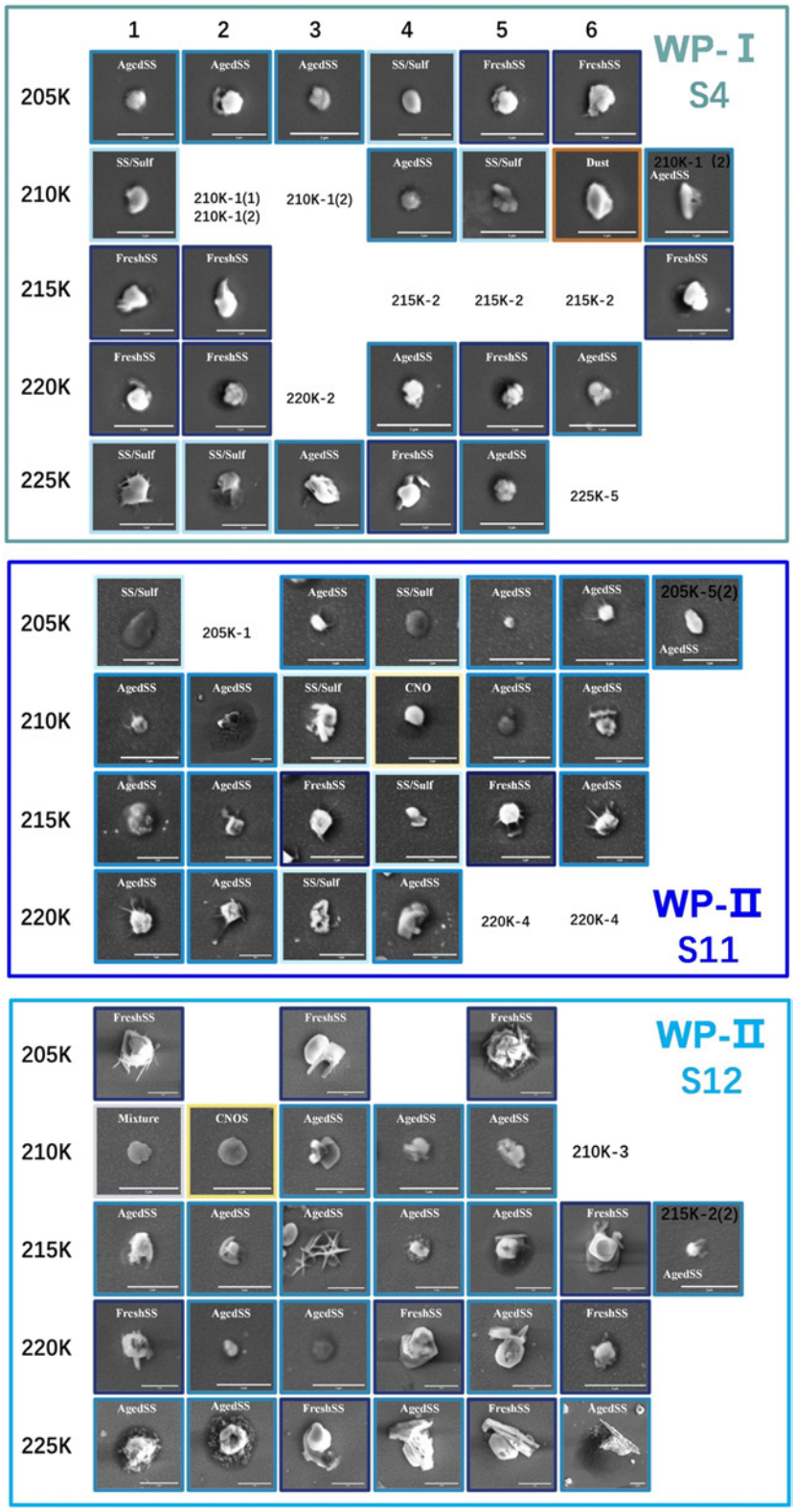

Figure S13. SEM images of INPs of the FreshSS and AgedSS dominated samples (S4, S11, and S12) identified at different freezing temperatures. Other descriptions of the labels are the same as in Figure S11 and Figure S12. The scale bar for all images is 2 μm.

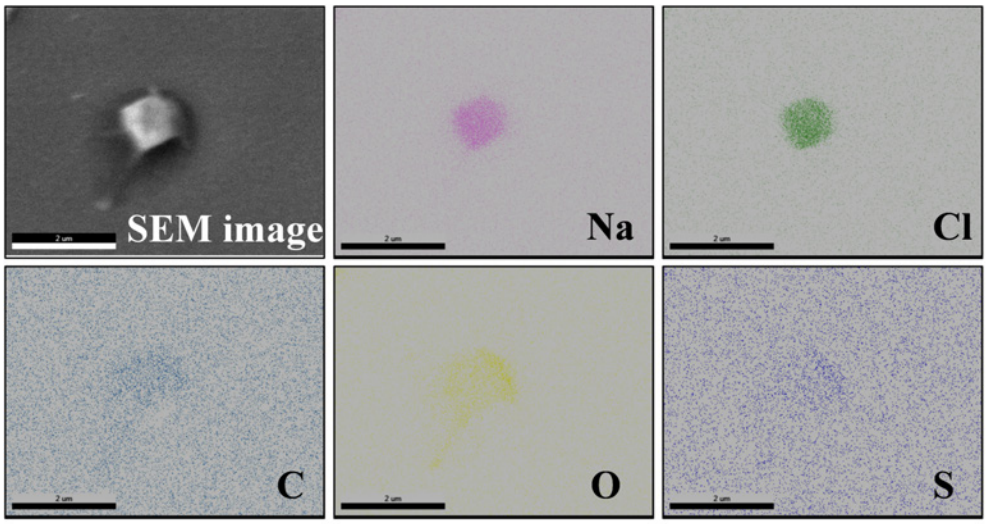

Figure S14. SEM image and EDX elemental maps for a typical AgedSS particle from S11 sample. The scale bar is 2 µm for all images.

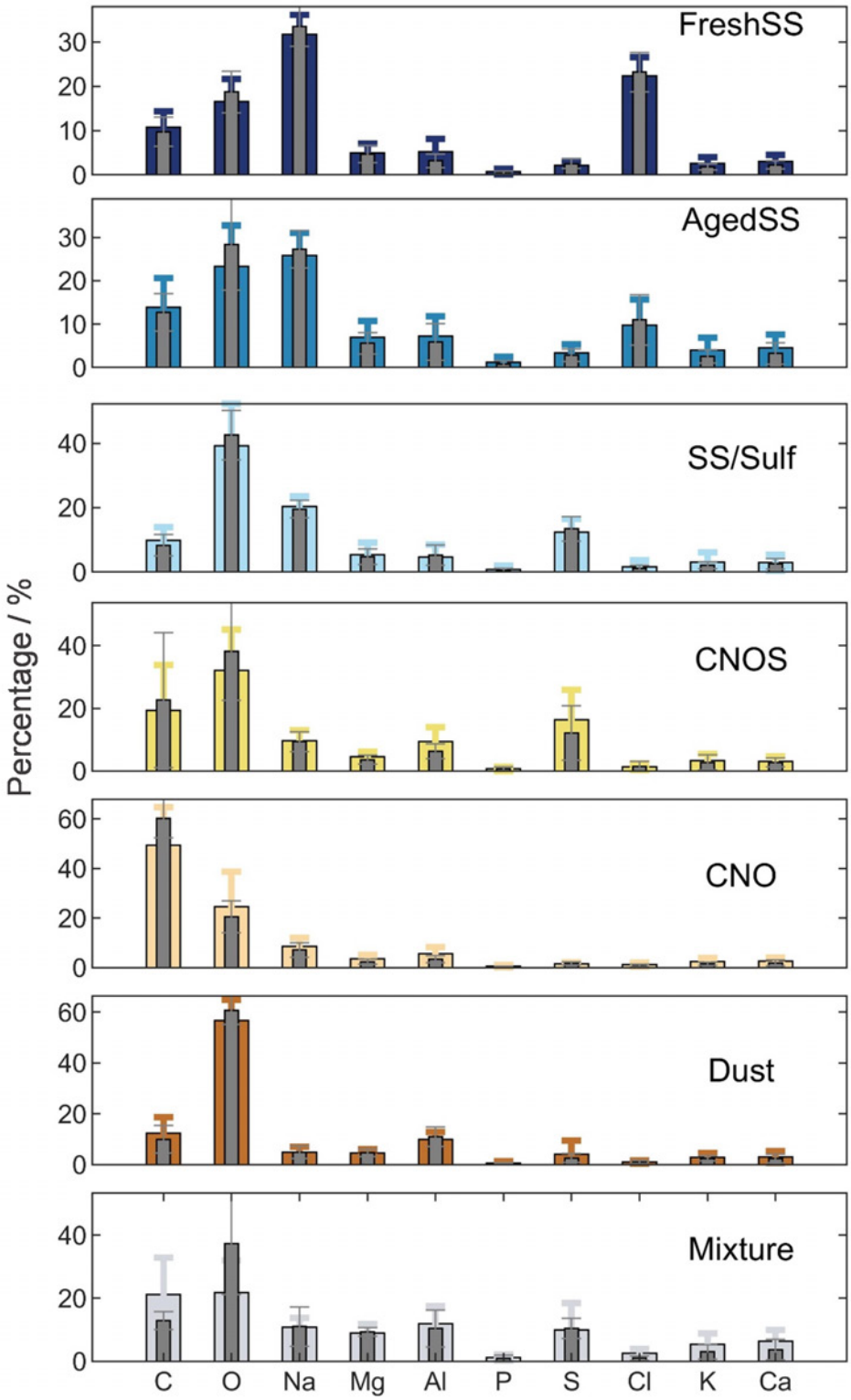

Figure S15. Elemental composition of INPs and non-INPs for each particle type (mean with one standard deviation). Narrow gray bars and wider color bars represent INPs and non-INPs, respectively.

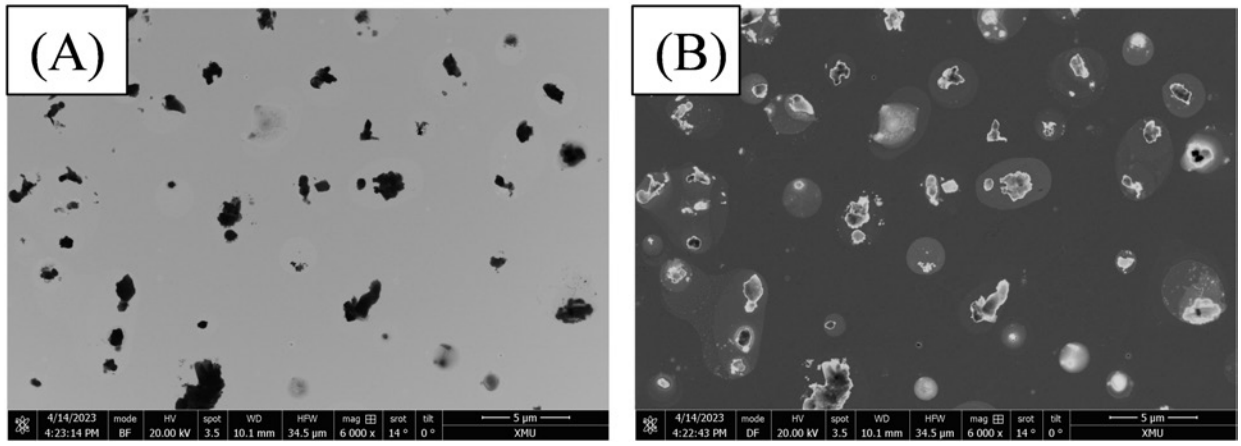

Figure S16. The SEM images of particles from S1 sample using scanning transmission electron microscopy (STEM) detector. (A) on the bright field mode, (B) on the dark field mode. The scale bar is 5 µm.

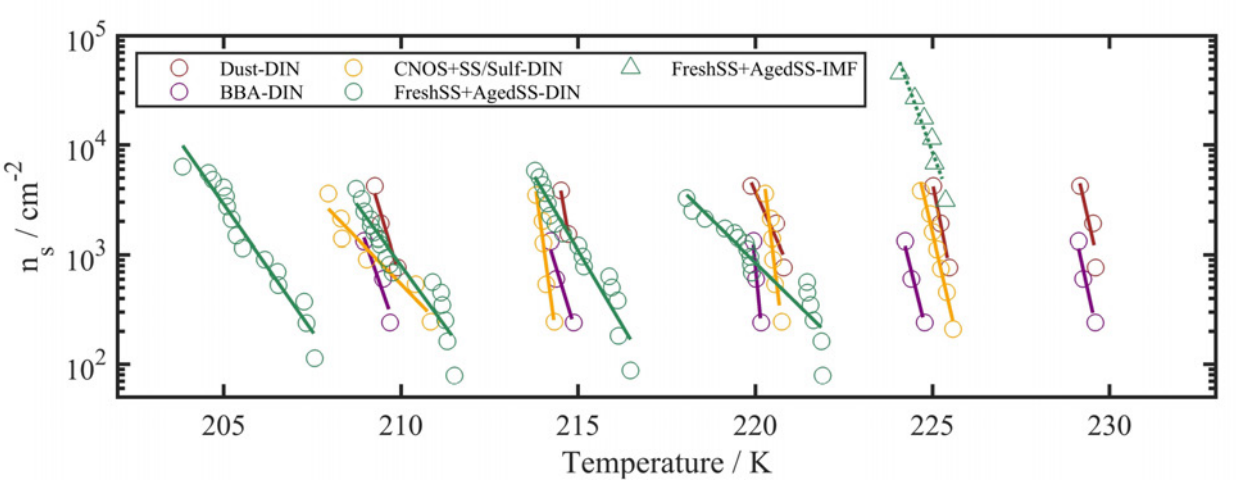

Figure S17. The n_s of all types of samples. Circles and triangles represent DIN and IMF, respectively. Lines indicate the fittings according to $\log_{10}(n_s) = a \times T + b$.

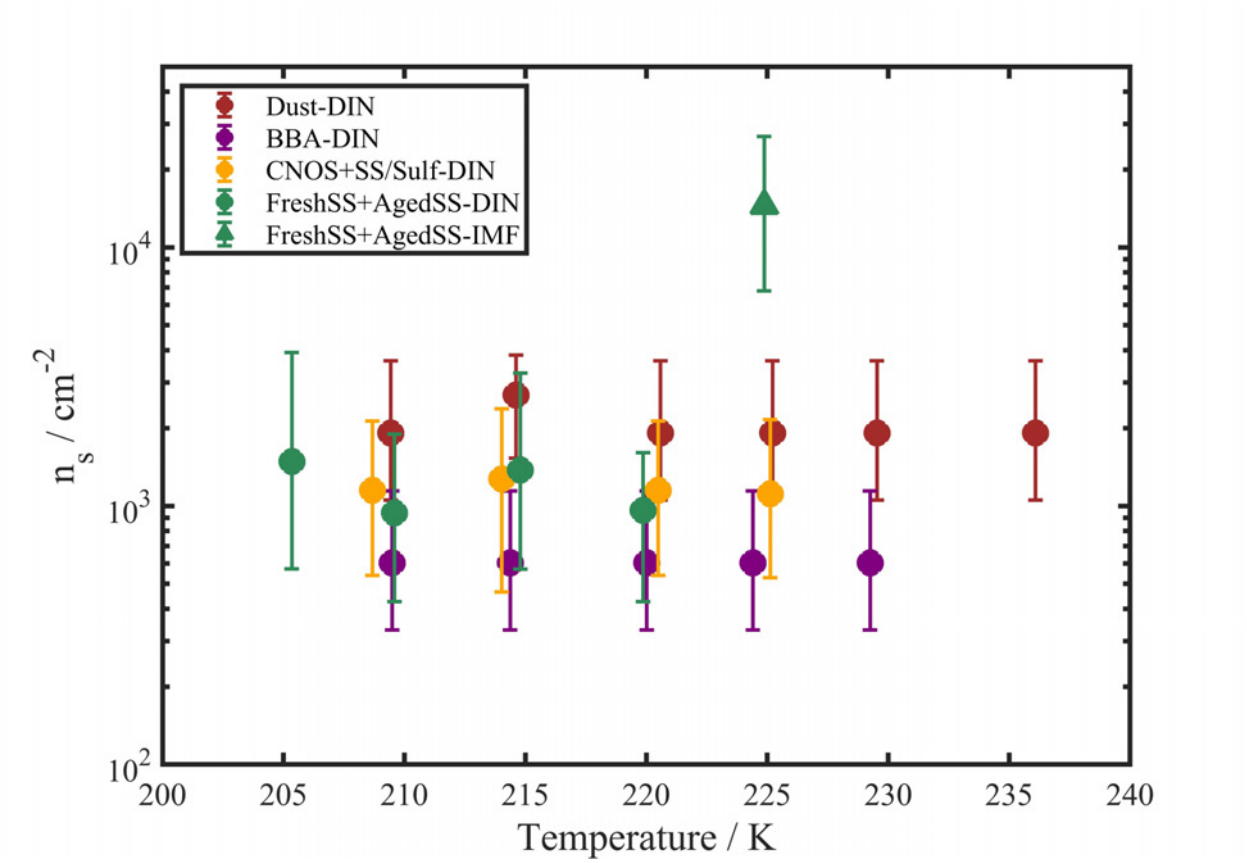

Figure S18. Median n_s with 25th and 75th percentiles for all types of samples. Circles represent DIN and triangles represent IMF. Brown, purple, orange, and green symbols represent Dust, BBA, CNOS and SS/Sulf, and the FreshSS and AgedSS dominated samples, respectively.

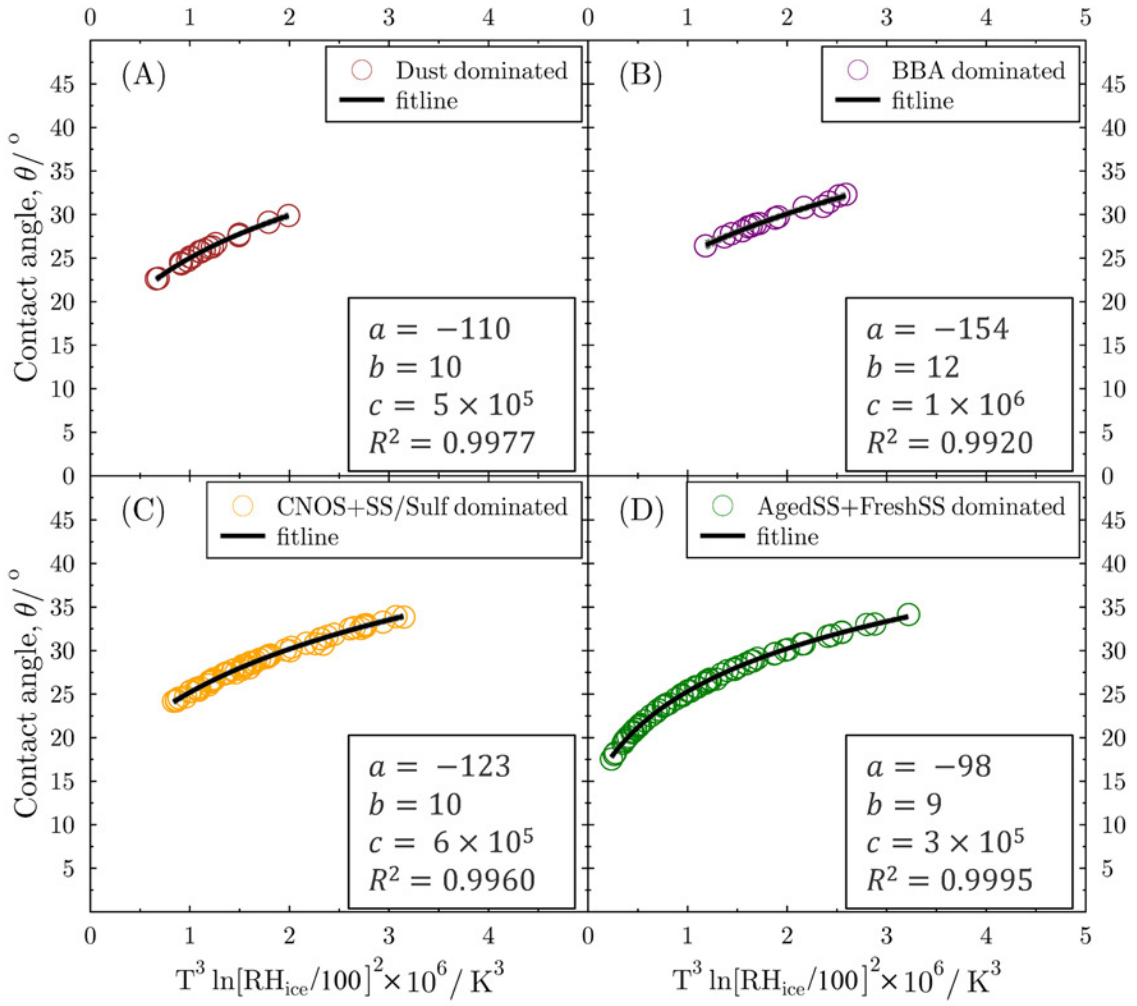

Figure S19. Parameterizations of θ as a function of $T^3 \ln[RH_{\mathrm{ice}}]^2$ including the ice nucleation onset temperature (T) and RH_{ice} for DIN by the Dust, BBA, CNOS and SS/Sulf, and the FreshSS and AgedSS dominated samples.

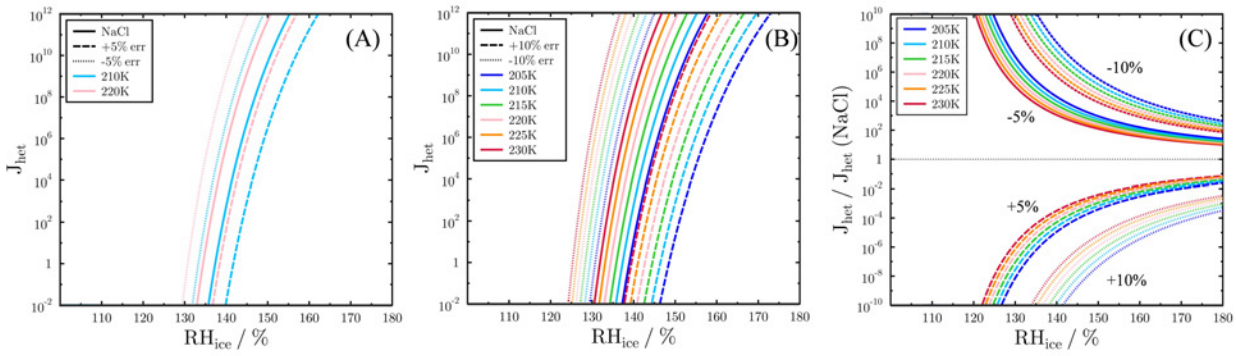

Figure S20. The DIN J_{het} that calculated based on CNT for NaCl, *Err* of ±5% (A) and *Err* of ±10% (B), and their ratio to J_{het} of NaCl (C) at different temperature and humidity conditions.

References:

Alpert, P. A. and Knopf, D. A.: Analysis of isothermal and cooling-rate-dependent immersion freezing by a unifying stochastic ice nucleation model, Atmos. Chem. Phys., 16, 2083–2107, https://doi.org/10.5194/acp-16-2083-2016, 2016.

China, S., Alpert, P. A., Zhang, B., Schum, S., Dzepina, K., Wright, K., Owen, R. C., Fialho, P., Mazzoleni, L. R., Mazzoleni, C., and Knopf, D. A.: Ice cloud formation potential by free tropospheric particles from long-range transport over the Northern Atlantic Ocean, J. Geophys. Res. Atmos., 122, 3065–3079, https://doi.org/10.1002/2016JD025817, 2017.

Connolly, P. J., Möhler, O., Field, P. R., Saathoff, H., Burgess, R., Choularton, T., and Gallagher, M.: Studies of heterogeneous freezing by three different desert dust samples, Atmospheric Chemistry and Physics, 9, 2805–2824, https://doi.org/10/bhhzwn, 2009.

Ghorai, S., Wang, B., Tivanski, A., and Laskin, A.: Hygroscopic properties of internally mixed particles composed of NaCl and water-soluble organic acids, Environ. Sci. Technol., 48, 2234–2241, https://doi.org/10.1021/es404727u, 2014.

Laskin, A., Moffet, R. C., Gilles, M. K., Fast, J. D., Zaveri, R. A., Wang, B., Nigge, P., and Shutthanandan, J.: Tropospheric chemistry of internally mixed sea salt and organic particles: Surprising reactivity of NaCl with weak organic acids, J. Geophys. Res., 117, 1–12, https://doi.org/10.1029/2012JD017743, 2012.

Vali, G.: Qauantitative evaluation of experimental results on the heterogeneous freezing nucleation of supercooled liquids, J. Atmos. Sci., 28, 402–409, https://doi.org/10.1175/1520-0469(1971)028<0402:QEOERA>2.0.CO;2, 1971.

Wang, B. and Knopf, D. A.: Heterogeneous ice nucleation on particles composed of humic-like substances impacted by O_3, J. Geophys. Res., 116, 1–14, https://doi.org/10.1029/2010JD014964, 2011.